Preprint Title	GO-Chl induce DNA damage in A549 lung cancer cells through SQSTM1/p62 mediated autophagy modulation
Authors	Braham Dutt Arya, Sandeep Mittal, Prachi Joshi, Alok K. Pandey, Jaime E. R. Vick, Govind Gupta and Surinder P. Singh
Publication Date	29 Aug. 2024
Article Type	Full Research Paper
Supporting Information File 1	Modified Supplementary Information DNA MS_BJNANO.docx; 2.3 MB
ORCID® iDs	Jaime E. R. Vick - https://orcid.org/0000-0001-9845-3734; Surinder P. Singh - https://orcid.org/0000-0002-8264-690X

GO-Chl induce DNA damage in A549 lung cancer cells through SQSTM1/p62 mediated autophagy modulation

Braham Dutt Arya, [1, 3†] Sandeep Mittal, [2, 3] Prachi Joshi, [1] Alok Kumar Pandey, [2, 3] Jaime E. Ramirez-Vick, [4] Govind Gupta,[1,3] and Surinder P. Singh [1, 3*]

[1]CSIR-National Physical Laboratory, Dr K. S. Krishanan Marg, New Delhi-12, India

[2]CSIR-Indian Institute of Toxicology Research (CSIR-IITR), 31, Mahatma Gandhi Marg, Lucknow-226001, India.

[3]Academy of Scientific & Innovative Research (AcSIR), New Delhi-20, India.

[4]Department of Biomedical, Industrial & Human Factors Engineering, Wright State University, Dayton, Ohio 45435, United States.

5Department of Higher Education, Shiksha Sadan, Sector-5, Panchkula-134114, India.

*Corresponding author email: singh.uprm@gmail.com

Abstract

Autophagy, a highly regulated catabolism for the degradation of unnecessary or dysfunctional cellular proteins. In response to endogenous or exogenous stresses the cancer cells use autophagy pathways for their survival through activation of complex DNA damage repair (DDR) mechanism. In the present study, we have demonstrated the genotoxicity induced in A549 lung cancer cells by exposure to the GO-Chl nanoconjugate and elucidated the role of autophagy modulation in harnessing the DNA damage response. GO-Chl causes loss of plasma membrane integrity, cell cycle arrest and significant genotoxicity in A549 cells. Further, elevated expression of key

autophagy proteins Beclin-1, ATG-7, LC3- I/II and SQSTM1/p62 reveal that inhibition of autophagy plays a crucial role in regulating the DDR capabilities of cancer cells. The results indicate that the interplay of DDR and autophagy pathways may open new paradigms for developing effective combinatorial nanodrug system against multidrug resistance cancers.

Keywords: Graphene oxide, Chloroquine, Autophagy, SQSTM1/p62, A549 cells, DNA damage.

1. Introduction:

Despite of advances in basic and clinical research, an increased mortality rate is seen worldwide in cancer associated deaths[1]. The heterogeneous and complex tumor microenvironment along with intrinsic and/or acquired drug resistance mechanisms like increased drug efflux, DNA damage repair, activation of pro-survival cell signaling cascades, alterations in drug targets moiety limits the effectiveness of chemotherapeutic treatment[2,3]. In general, chemotherapeutic drugs inhibit the cancer progression and metastases by directly or indirectly targeting DNA of cancer cells, inducing a variety of DNA lesions. Cancer cells are equipped with complex molecular signaling pathways for recognition and repair of damaged DNA[4]. The activation of the DNA damage response (DDR) machinery by phosphatidylinositol 3-kinase-related kinase (PIKKs) family proteins, like ataxia telangiectasia-mutated and Rad3-related (ATR) and DNA dependent protein kinase catalytic subunit (DNA-PKcs), upon exposure to chemotherapeutics is a major hurdle in the treatment of chemoresistance tumors due to its complexity and redundancy[5]. Various pre-clinical studies have shown that inhibition of DDR either through autophagy modulation or PARP inhibition could provide a better therapeutic response[6,7].

Recently, nanomedicine has shown immense potential/efficacy in treatment of chemoresistant tumors by providing improved molecular targeting, better pharmacokinetics, and reduced side

effects. Nanomaterials can directly target DNA or inhibit the DDR and sensitize cancer cells to chemotherapeutics in multi-drug resistant tumors[8–10]. Satapathay, et al., reported DNA damage and apoptotic cell death in HCT116 colon cancer cells after exposure to starch-capped silver nanoparticles (AgNPs)[11]. Gemcitabine encapsulated PLGA nanoparticles have been shown an enhancement in chemo-resistant PANC1 cell death[12]. Also, TiO_2 nanoparticles can sensitize A549 lung carcinoma epithelial cells towards the genotoxic agent methyl methanesulphonate through disruption of the DDR process[13]. Recently, ZnO nanoparticles induced significant cytotoxicity and DNA double strand breaks in SKOV3 human ovarian cancer cells through induction of oxidative stress and autophagy modulation[14].

Graphene oxide (GO) due to its unique physico-chemical properties has attracted vast scientific attention as an efficient drug delivery carrier and modulator of biological activities, including autophagy, DDR, and intracellular transportation of therapeutics into cancer cells [15–17]. GO exposure has been shown to trigger autophagy response through toll-like receptors in CT26 colorectal carcinoma cells, and lysosomal destabilization in PC12 pheochromocytoma cancer cells, leading to cell death[18,19]. GO has been shown to sensitize CT26 (colorectal), Skov-3 (ovarian), HeLa (cervical), and Tramp-C1 (prostatic) cancer cells to chemotherapeutics through enhanced acetylation of histone in the nucleus causing increased decondensing of chromatin and making cancer cells more susceptible to DNA damage[15]. GO has also been shown to selectively target cancer stem cells among multiple cell types by inhibiting a number of different signal transduction pathways, including WNT, Notch, STAT 1/3 and NRF-2, respectively[20]. GO nanosheets have been shown to selectively disrupt the cell membrane and cytoskeleton of cancer cells through activation of FAK-Rho-ROCK pathway and suppressed expression of integrin[21]. It has also been found that nuclear accumulation of p62, due to inhibition of autophagy in cancer

cells, subsequently suppresses chromatin and histone ubiquitination and inhibits the DDR mechanism[22]. Cancer cells are known to employ autophagy in response to DNA damage as a survival mechanism and inhibition of autophagy could be an excellent treatment modality in multidrug resistant tumors[23,24] . Recently, it has also been found that chloroquine (Chl, autophagy inhibitor) conjugated GO induces necroptotic cell death in A549 cells through accumulation of p62 mediated by altered autophagic flux, reactive oxygen species (ROS) level and activation of RIPK1[25]. In the present study, we have investigated the DNA damage mediated cell death mechanism in A549 cells on exposure of Graphene oxide -Chloroquine (GO-Chl) nanoconjugate. Our results have shown that exposure of GO-Chl nanoconjugate induced DNA fragmentation/damage in A549 cells, causing significant genotoxicity which ultimately leads to enhanced cancer cell death[25]. Further, we have analyzed the meaningful partnership between autophagy modulation and DNA damage in GO-Chl exposure A549 cells. Furthermore, immunoblot analysis of autophagy biomarkers reveals the relationship between autophagy and DNA damage in response to GO-Chl exposure of adenocarcinomic human alveolar basal epithelial (A549) cells.

2. Experimental Section

2.1 Materials

Graphite powder, Chloroquine, 3-[4,5-dimethylthiazol-2-yl]-2,5-diphenyltetrazolium bromide (MTT), 5,5', 6,6'-Tetrachloro-1,1',3,3'-tetraethyl- benzimidazolecarbocyanine iodide (JC-1) dye, paraformaldehyde (PFA), Dimethyl sulfoxide (DMSO), Triton X-100, monodansylcadaverine (MDC), anti-SQSTM1 and anti-MLKL primary antibody, protein A/G agarose beads, Hydrogen peroxide (H_2O_2) from Sigma Aldrich (t. Louis, MO, USA). Phosphate buffered saline (Ca^{+2}, Mg^{+2} free; PBS), Dulbecco's modified eagle medium: nutrient mixture F-12 (Ham) (1:1) powder

(DMEM F-12), trypsin-EDTA, fetal bovine serum (FBS), antibiotic and antimycotic solution, secondary antibodies conjugated to HRP were purchased from Life Technologies (Invitrogen, Carlsbad, CA, USA). A549 human lung adenocarcinoma cells were obtained from American Type Cell Culture (ATCC, Manassas, VA, USA). Primary antibodies anti-β-actin, anti-LC3, anti-Atg7 and anti-beclin1 were obtained from Cell Signaling Technology (Danvers, MA, USA). Plasmid GFP-LC3 was a kind gift from Dr. Soumya Sinha Roy, CSIR-IGIB, India. Antifade mounting media Vectashield was purchased from Vector Laboratories (Burlingame, CA, USA). All other chemicals were obtained locally and were of analytical reagent grade. Cell culture plastic wares were obtained from Thermo Scientific Nunc (Rochester, New York).

2.2 Synthesis of Graphene oxide

Highly exfoliated GO nanosheets were chemically synthesized using a modified Hummer's method[26,27]. Briefly, 0.5 g of graphite powder was treated with a mixture of 0.5 g $NaNO_3$ and 40 mL H_2SO_4 (98%) that intercalates between graphitic layers. Finely powdered $KMnO_4$ (1.5 g) was slowly added (time span ~ 30 min) to the reaction mixture under continuous stirring at 4°C in an ice bath (0-5°C). The reaction mixture kept under vigorous stirring for 12 h at room temperature, until a dark brownish precipitate appears, followed by addition of 1.5 mL of H_2O_2 (30%) and 100 mL ice cold ultrapure water to stop the oxidation reaction and eliminate unreacted $KMnO_4$. The chemistry involved in the chemical exfoliation of graphite is shown in Figure S1 (supplementary information). The purified graphitic sheets were collected using successive centrifugation at 13,000 rpm for 30 min and washing with Deionized (DI) water several times, until hydrolysis of covalent sulfates formed during oxidation[28]. The final product of exfoliated GO nanosheets were extracted through freeze drying.

2.3 Binding of Chloroquine onto Graphene oxide nanosheets

Chloroquine molecules were bound to the GO nanosheets through non-covalent π-π interactions between quinoline of Chl and graphitic domain of GO, according to previously reported procedure[25]. Briefly, 100 mL aqueous dispersion of GO (500 μg/mL) nanosheets was mixed with 15 mL of aqueous solution of Chl diphosphate (250 μg/mL) under continuous stirring at room temperature in dark for 24 h. The final GO-Chl nanoconjugate was collected by centrifugation at 9500 rpm for 15 min followed by freeze drying. The supernatant was separated for quantitative estimation of the unbound drug.

2.4 Physical characterization techniques

The functional group and structural analysis of GO and GO-Chl nanoconjugate were studied using a Fourier transform infrared spectrometer (Cary 630 FTIR, Agilent, CA, USA) in ATR mode and a Raman spectrophotometer (Ranishaw win-via reflex spectrometer, Tokyo, Japan) with a 514 nm Nd:Yag laser as an excitation source. The optical properties were measured employing a UV–Vis spectrophotometer (Cary 5000 UV-VIS-NIR, Agilent, CA, USA) in the 200-800 nm range. The morphology of GO nanosheets were analyzed employing high resolution transmission electron microscope (Technai G2 F30 STWIN, Japan), field emission scanning electron microscope (FEI, Quanta FEG 450, USA) and atomic force microscopy (Nanoscope, Veeco V, USA).

2.5 Cell culture

Human lung adenocarcinoma cells (A549) from the American Type Culture Collection (ATCC, Manassas, VA, USA) were cultured using DMEM F-12 medium (Life Technologies, Invitrogen, Carlsbad, CA, USA), supplemented with 10% heat inactivated fetal bovine serum, 0.2% sodium bicarbonate, and 10 mL/L antibiotic and antimycotic solution. The cells were maintained at 37°C

under a humidified atmosphere of 5% CO_2. Cells were seeded in 96-well plates, 12-well plates and 75 cm^2 culture flasks, depending on the experiment and were grown overnight. Then, fresh medium with varying concentrations (1–100 μg/mL) of GO–Chl nanoconjugates was added to the cells and incubated for a time period, which depended on the specific experiment. Each group contained four technical replicates and three biological replicates for each experiment. In each assay cells without nanoconjugates were used as a control.

2.6 PI uptake analysis

Propidium iodide (PI), a positively charged nucleic acid dye, specifically exhibits fluorescence after binding with DNA of cells with compromised membrane and used for quantitative estimation of plasma membrane integrity using flow cytometry[29]. Briefly, A549 cells (1×10^5 cells/mL/well) were seeded in 12 well culture plates and exposed to varying concentrations (1 - 100 μg/mL) of GO-Chl for 24 h. Cells were washed with 1× PBS, harvested using 0.25% trypsin and centrifuged at 1000 rpm for 10 min to remove excess GO-Chl nanoconjugate. Furthermore, cells were resuspended in 100 μL of 1× PBS and incubated with PI dye (stock: 1 mg/mL; working: 2 μL/100 μL) for 10 min at room temperature in the dark. Further, cell suspension was diluted by adding 400 μL of 1× PBS and red fluorescence emitted from PI was analyzed by flow cytometry (BD FACS Canto II, BD Biosciences, San Jose, CA, USA) using a 650±13 nm band pass filter. Three independent experiments were performed for each group. The proportion of cells with compromised membrane integrity was analyzed using FACS Diva software (version 6.1.2, BD Biosciences, San Jose, CA, USA). Values represent mean ± standard error (SE) of three independent experiment. A value of $p < 0.05$ (*) was considered as statistically significant.

2.7 Cell cycle analysis

The cell cycle analysis was carried out by flow cytometry using PI[29]. Briefly, A549 cells were treated with different concentrations (1–100 μg/mL) of GO-Chl nanoconjugate for 24 h. Cells were washed twice with cold 1× PBS, harvested using 0.25% trypsin, centrifuged at 1000 rpm for 10 min, and the pellet was resuspended in 300 μL of 1× PBS. Furthermore, cells were fixed with 70% ice cold ethanol and incubated overnight at -20°C. Thereafter, cells were centrifuged at 1200 rpm for 4 min and the resulting pellet was resuspended in 200 μL of lysis buffer (1× PBS along with 0.2% Triton X-100) and incubated at 4°C for 30 min. Lysed cells were then treated with RNase (10 mg/mL) for 30 min at 37°C to eliminate the RNA as PI can binds to double-stranded RNA. Finally, cells were once again centrifuged at 1200 rpm for 10 min and the pellet was resuspended in 500 μL of 1× PBS containing 10 μL of PI dye (1 mg/mL) and stored at 4°C until analysis using flow cytometry. Three independent experiments were performed for each group. Values represent mean ± SE of three independent experiment. A value of $p < 0.05$ (*) was considered as statistically significant.

2.8 Comet assay/single cell gel electrophoresis for DNA damage analysis on exposure of A549 cells to GO-Chl nanoconjugates

Single cell gel electrophoresis was used to investigate the DNA denaturation and single strand DNA breaks upon exposure of A549 lung cancer cells to GO-Chl nanoconjugates. For quantitative estimation of DNA damage, we followed the method developed by Singh, et al.,[30] and base slides were prepared according to the method of Bajpayee, et al.[31]

Briefly, A549 cells (1×10^5 cells/mL/well) were seeded in 12 well culture plates and exposed to varying concentrations (1-100 μg/mL) of GO-Chl for 6 h. Cells were washed twice with 1× PBS

to remove any GO-Chl nanoconjugate not up taken by the cells. Cells were then harvested using trypsin-EDTA and resuspended in 100 μL of 1× PBS, followed by mixing with 1% low melting point agarose (LMPA, prepared in 1× PBS) to achieve a final concentration of 0.5%. Thereafter, 80 μL of the suspension were layered on base slide (pre coated with 1% normal melting agarose; NMA), evenly spread with a cover slip and kept on ice to allow gelation. The cover slip was carefully removed followed by addition of a third layer of 90 μL of 0.5% LMPA, carefully spreading with a cover slip and kept on ice to allow gelation.

Duplicate slides for each sample were prepared and were kept in freshly prepared and chilled lysis solution (146.1 g NaCl, 37.2 g EDTA, 1.2 g Tris, pH 10 with 1% Triton X 100 added just before use) at 4°C overnight. Further, the slides were placed in a horizontal gel electrophoresis tank containing freshly prepared chilled electrophoresis solution (1 mM EDTA, 300 mM NaOH, pH > 13) for 20 min for DNA unwinding and subsequently subjected to electrophoresis with 300 mA current, 0.7 V/cm at 4°C under dimmed light for 30 min. After electrophoresis, the slides were treated with Tris buffer (0.4 M, pH 7.5) 3× at 5 min per cycle to neutralize excess alkali solution, stained with 75 μL of ethidium bromide (20 μg/mL) and stored in a humidified slide box until scoring. The slides were scored using a fluorescent microscope (DMLB, Leica, Germany) coupled with CCD camera and image analysis system (Andor Technology, Belfast, UK) and software (KOMET 5.0, Kinetic Imaging, UK) at 400× magnification. Three independent experiments were performed for each group. The mean value of three Comet parameters, tail DNA (%), tail length (μm) and Olive tail moment (OTM) were considered during the analysis. Values represents mean ± SE of three independent experiments. A value of $p < 0.05$ (*) was considered as statistically significant.

2.9 Autophagy analysis

The effect of GO-Chl exposure on autophagy modulation in A549 cells was studied employing the following assays:

2.9.1 MDC Staining

Fluorescent monodansylcadaverine (MDC) selectively accumulates in acidic vacuoles and has been used as a tracer for autophagic vacuoles[32]. Briefly, A549 cells were plated on 20 mm round-glass cover slips and allowed to adhere overnight. Next day, cells were exposed to 25 μg/mL GO–Chl nanoconjugate (dose chosen based on cell death analysis in our previous study[25]) for 24 h, rinsed with 1× PBS and stained with 50 mM MDC at 37 °C for 1 h. Finally, cells were washed with 1× PBS, and the cellular fluorescence changes were observed using Nikon Eclipse Ti-S inverted fluorescent microscope equipped with Nikon Digital slight Ds-Ri1 CCD camera and NIS element BR imaging software (Nikon, Minato Tokyo, Japan). Three independent experiments were performed for each group and a representative image is shown in the results.

2.9.2 Transfection of GFP-LC3 plasmid

GFP-LC3 plasmids were employed to evaluate the quantitative formation of autophagic puncta upon GO–Chl exposure[33]. Briefly, A549 cells were plated in 4 well chamber slides and transiently co-transfected with mammalian GFP-LC3 plasmid employing conventional lipid-mediated gene delivery reagent lipofectamine 2000 following manufacturer's instructions. After 6 h, the transfection medium was replaced with fresh medium and cells were incubated overnight. Cells were then exposed to 25 μg/mL GO–Chl for 24 h and washed with 1× PBS. The cells were then fixed in 4% paraformaldehyde at 4°C for 30 min, mounted using antifade and analyzed using confocal microscopy.

2.10 Immunoblot analysis

The expression level of various autophagy related proteins to investigate the autophagy process were analyzed using immunoblotting analysis. Briefly, A549 cells (5×10^5 cells/flask) were seeded in 25 cm^2 culture flask and exposed to different concentrations (1-100 μg/mL) of GO-Chl nanoconjugate for desired time. Cells were washed twice with cold 1× PBS, harvested and the whole-cell extract was prepared using a cell lytic reagent (Sigma-Aldrich, St. Louis, Missouri, USA) supplemented with protease and phosphatase inhibitors. Protein content was quantitated using the Bradford assay and further resolved by sodium dodecyl sulfate–polyacrylamide gel electrophoresis (SDS-PAGE)[34], transferred to a polyvinylidene difluoride (PVDF) membrane by electroblotting, blocking with casein-blocking buffer (Sigma-Aldrich) for 1 h at room temperature, and incubation with primary antibodies in 1× TBST overnight at 4°C. Next day, blots were washed with 1× TBST and incubated with the corresponding horseradish peroxidase-coupled anti-rabbit or anti-mouse secondary antibodies (Cell Signaling Technology, MA, USA). Proteins were visualized with Super Signal West Femto reagents (Pierce Biotechnology, Rockford, IL, USA) through chemiluminescence. Three independent experiments were performed for each group. Values represents mean ± SE of three independent experiment. A value of $p < 0.05$ (*) was considered as statistically significant.

3. Result and Discussion:

3.1. Physical characterization analysis

The synthesis of graphene oxide involves chemical exfoliation and oxidation of graphite powder employing modified Hummer's method[27] as shown in Figure 1. The chemical synthesis of highly pure graphene oxide nanosheets depend on several factors like source of graphite, weight

equivalent of $KMnO_4$, reaction time and washing conditions[28,35]. Most importantly, the degree of oxidation of graphene oxide plays a crucial role in controlling the cytotoxicity of the material[36,37]. To achieve higher oxidation, 6 weight equivalent of $KMnO_4$ (added in two steps of 3 eq. each) were used relative to graphite powder used. Chloroquine binds to the surface of graphene oxide nanosheets through non-covalent π–π interactions between the quinoline ring of Chl and sp^2 hybrid π-bonded carbon framework of graphene oxide.

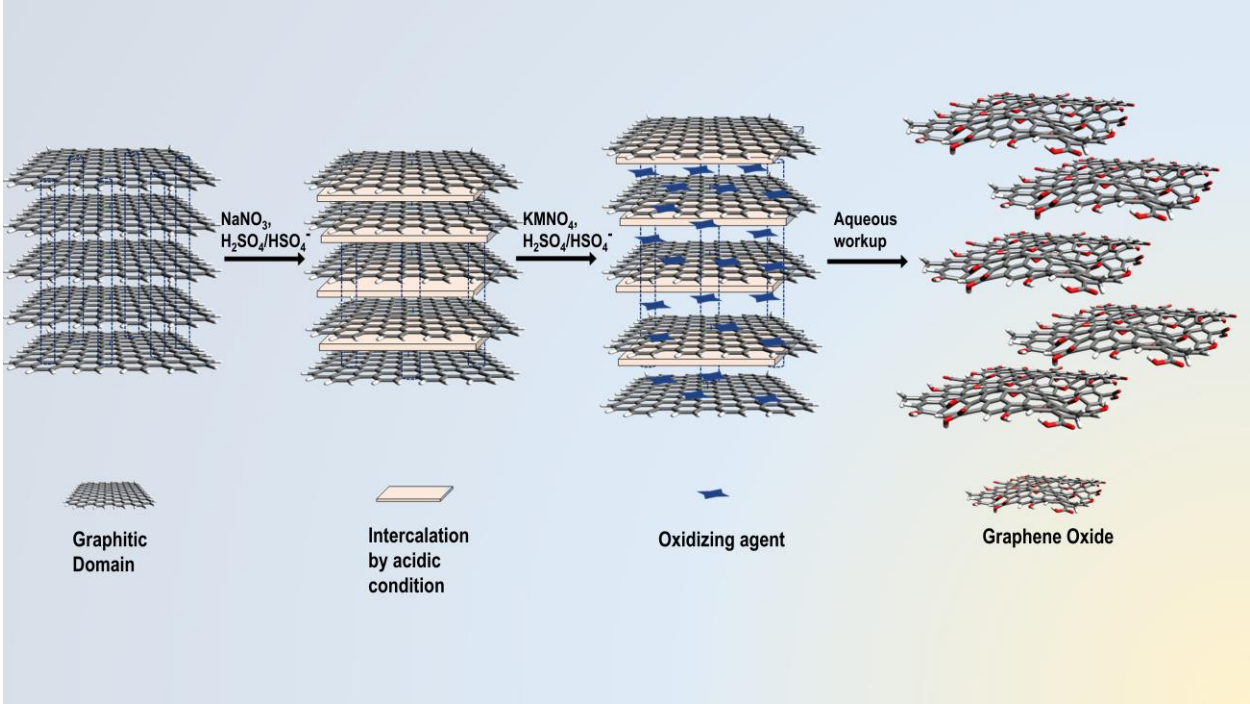

Figure 1. Schematic representation for the process of chemical exfoliation and oxidation of graphite powder to obtained highly exfoliated graphene oxide nanosheets. (Fig. 1 was created by the authors using Avogadro: an open-source molecular builder and visualization tool. Version 1.0.2n http://avogadro.cc/)[38]

The formation of GO-Chl nanoconjugates was confirmed by investigating the optical, functional, structural, and morphological properties employing standard analytical characterization techniques. The optical properties of GO and GO-Chl were assessed using UV-Vis spectroscopy

(supplementary information). Figure S1a, reveals the appearance of characteristic bands around 230 nm and 295 nm for GO which corresponds to π–π* to and n–π* electronic transitions, respectively. The observed high intensity π–π* plasmon peak around 230 nm is attributed to well defined nanoscale sp^2 hybrid π-bonded networks and chromophore aggregation due to presence of C=C, C=O and C–O bonds[39]. The presence of a shoulder band around 295 nm corresponds to the well-defined n–π* electronic transitions due to the presence of C=O functional groups on the surface of GO. The appearance of the Chl characteristic band at around 343 nm, in GO-Chl, could be related to the binding of Chl to GO[40].

The functional groups in GO and GO-Chl nanoconjugates were analyzed by FTIR spectroscopy. Figure S1b shows the FTIR spectrum of GO, Chl and GO-Chl in the range of 500-3800 cm^{-1}, respectively. The presence of broad peak around 3200-3400 cm^{-1} and other characteristic bands around 1720 cm^{-1}, 1620 cm^{-1}, 1150 cm^{-1} and 1050 cm^{-1} for GO, which correspond to the stretching vibration of –OH, C=O, C=C, C-OH and C(O)C bonds, respectively[28,41]. The appearance of a peak around 2980 cm^{-1} in both Chl and GO-Chl corresponds to the C-H stretch of methyl group present in Chl and GO-Chl, respectively. Furthermore, the presence of C-N stretch (1360 cm^{-1}), N-H bending of amine and C-Cl stretch (530 cm^{-1}) in Chl and GO-Chl reveals the formation of GO-Chl nanoconjugate[25,42].

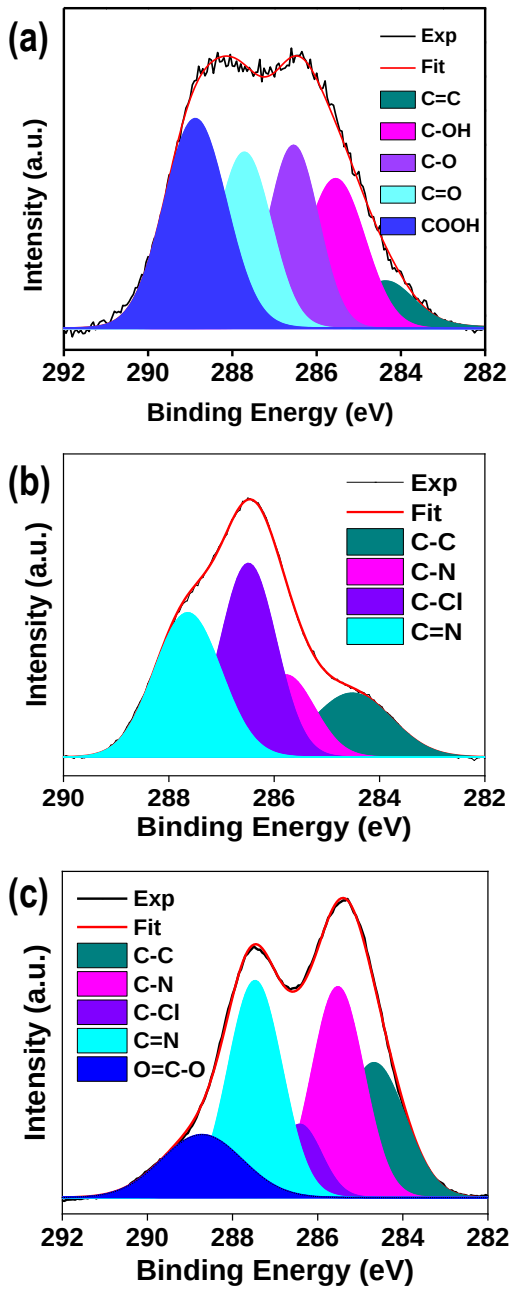

Figure 2. X-Ray photoelectron spectroscopic analysis. C 1s core level spectra for GO (a), Chl (b) and GO-Chl (c), respectively. Experimental (black line), fitted data (red line) and deconvoluted fitting components (multicolored regions) are also shown here.

Furthermore, the chemical states/structures of GO, Chl and GO-Chl were investigated through X-ray photoelectron spectroscopy. Figure 2a-2c, correspond to the deconvoluted C (1s) core level of GO, Chl and GO-Chl respectively. To analyze the relative content of functional groups, the C (1s) peaks of the samples were deconvoluted into different components viz C=C (284.4), C-N (285.5), C-OH (285.6), C-Cl (286.3), C-O (286.6), C=N (287.2), C=O (287.7) and COOH (288.8) eV, respectively, using the Voigt (mixed Gaussian-Lorentzian) function. The peak fitting was performed with respect to the chemical bonding of materials, least count of the instrument and due agreement with the available literature[43,44]. The appearance of high intensity functional group peaks (286-290 eV) relative to C–C sp^2 framework peak (graphitic domains, 284.4 eV) in GO indicates the formation of highly exfoliated and oxidized GO nanosheets[43]. The deconvoluted C (1s) core level peaks of GO with the relative intensity of 30.2 % (COOH), 21.5 % (C=O), 20.8 % (C-O), 20.2 % (C-OH) in comparison to 7.3 % (C=C) confirms the high content of oxygen containing functional group on the surface of GO nanosheets. In contrast, the deconvoluted C (1s) core level of GO-Chl reveals the presence of GO and Chl associated C=C, C-N, C=N, C-Cl and COOH functional groups in the GO-Chl nanoconjugate. The observed reduction in intensity of COOH peaks for GO-Chl, as compared to GO, could be attributed to the possible reduction of oxygen rich functional groups as a result of their interaction with amino groups present in Chl[45]. It was observed that the GO-Chl sample shows the prevalence of C-N and C=N states, while C-Cl and C=N bonds were more dominant in Chl. These observations are in good agreement with our previously reported FTIR-based analysis. Also, the presence of C=N peaks in Chl and GO-Chl indicates the presence of amino domains of Chl onto GO-Chl nanoconjugate. Observed data with relative % are shown in table S1 (supplementary information).

The morphological analysis of GO was carried out using field emission scanning electron microscopy (FESEM) and high-resolution transmission electron microscopy (HRTEM). In figure S1d, the FESEM image reveals a well-defined interlocked 3D network of GO nanosheets, with the transparency observed attributed to the formation of single or few layered GO nanosheets[25,46]. In figure S1e, the HRTEM micrograph reveals highly transparent GO nanosheets with few wrinkles and folds and corroborates the FESEM observation for formation of single or few layered GO nanosheets[47]. The selected area electron diffraction pattern of GO shown in figure S1f, leads to the observation of a 6-fold clear diffraction spot pattern, characteristic of hexagonal crystalline lattice, indicating GO not being completely amorphous. In addition, the absence of any additional spots other than graphitic structure suggests that oxygen containing functional groups in GO does not contribute to form-ordered lattice arrangements[47,48]. These spectroscopic and morphological results were in good agreement with our previous observations[25].

3.2 Quantitative Estimation of Chl binding onto GO nanosheets

The amount of Chl bound onto GO sheets was estimated in two ways viz entrapment efficacy (EE, % Chl that has been successfully absorbed onto GO) and % drug content or drug loading efficiency (DLE, amount of Chl loaded per unit weight of GO) using UV–Vis spectroscopy. Firstly, a standard calibration curve of Chl was plotted by monitoring the optical density at 343 nm (as shown in Figure 3a) and concentration of Chl present in GO-Chl nanoconjugate was calculated using the calibration curve. EE and DLE were calculated using Eq. 1 and 2 and the results are summarized in Table 1.

$$\text{Entrapment Efficacy (EE)} = \frac{(A-B)}{A} \times 100 \quad (1)$$

where A and B are the total amount of drug used in 115 mL of solution and amount of unbound drug left in supernatant, respectively.

$$\text{Drug Loading Efficiency (DLE)} = \frac{(m_o - m_{sup})}{m_{GO}} \times 100\% \quad (2)$$

where m_o, m_{sup} and m_{GO} are total amount of drug used initially, unbound drug obtained in supernatant and weight of GO, respectively.

Table 1. Estimation of entrapment efficacy (EE) and drug loading efficiency (DLE) using UV-Visible spectroscopy

S. NO.	*Total amount of Chl used in 115 mL (A)*	*Total amount of Chl per mL*	*OD of supernatant*	*Amount of drug left in supernatant (From OD) (B)*	*EE =* $\frac{(A-B)}{A} \times 100$	*DLE =* $\frac{(m_o - m_{sup})}{m_{GO}} \times 100\%$
1	7500 µg in 115 mL	65.217 µg/mL	0.270	7.5 µg/mL	88.49	6.637 %

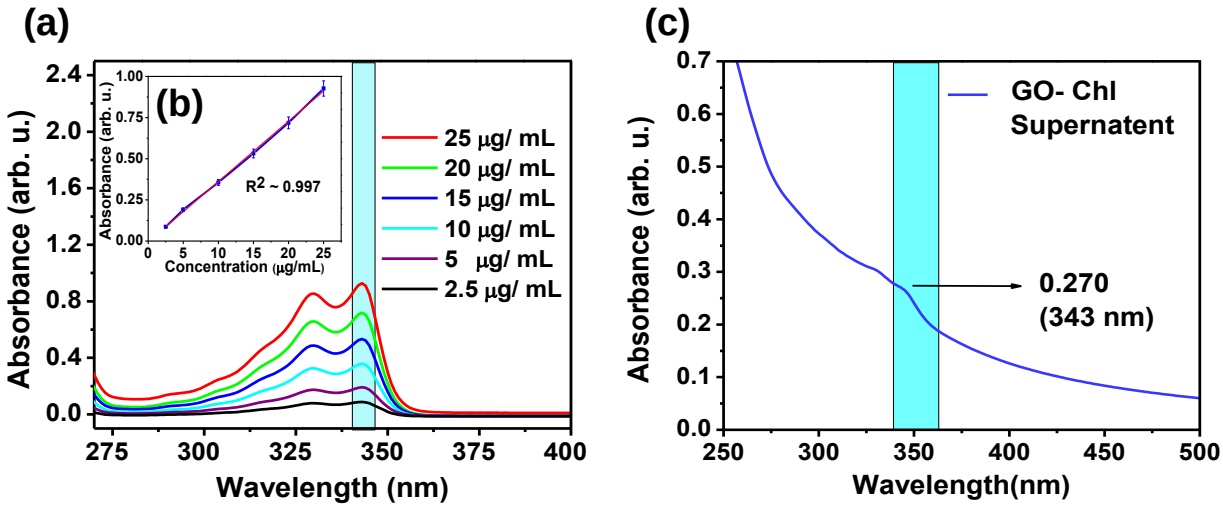

Figure 3. Quantitative estimation of Chl binding onto GO nanosheets using UV-Vis spectroscopy: (a) Optical density measurement of various concentration (2.5 – 25 µg/mL) of Chl for preparation of standard calibration curve, (b) Linearity plot (R^2 ~ 0.997) prepared by measuring relative optical density for different concentration of Chl and (c) optical density measurement of supernatant having unattached Chl.

3.3 Cellular Internalization of GO-Chl nanoconjugate and Flow cytometry-based PI uptake analysis

The efficacy of nanomedicine mainly depends upon the effective cellular internalization and its transport to the appropriate intercellular effector site[49]. Studies have shown that based on its size and surface characteristics (like hydrophilic or hydrophobic, and C/O ratio) GO is internalized via clathrin or caveolae-mediated endocytosis and micro-pinocytosis[50]. Exposure to nanomaterials is known to affect plasma membrane integrity, which in turn initiates various metabolic processes, like ineffective nutrient transport, unspecific molecular targeting, DNA damage, and dysfunction of other intracellular organelles[49,51]. In Figure 4, TEM micrographs reveal the presence and

effective cellular internalization of the GO-Chl nanoconjugate in A549 cells, corroborating our previous findings[25].

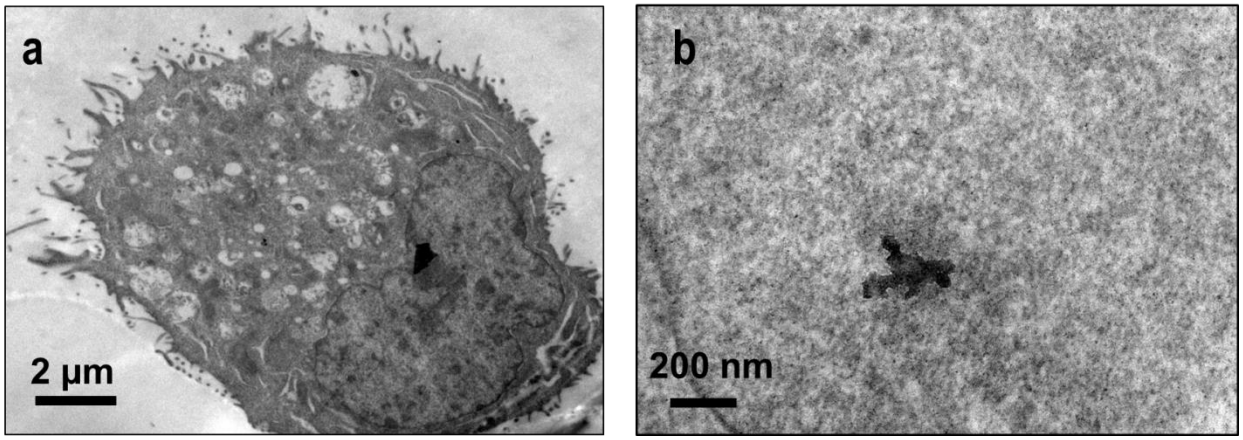

Figure 4. Cellular internalization of GO-Chl nanoconjugates: (a-b) Transmission electron microscopy analysis of GO-Chl nanoconjugate in A549 lung cancer cells at different magnifications.

To investigate the effect of GO-Chl on plasma membrane integrity and cells viability, we performed flow cytometry-based PI uptake analyses. Figure 5 reveals the dose dependent increase in the number of cells with compromised membranes, which indicate significant growth in the number of dead A549 cells after exposure to GO-Chl. These results are in good agreement with our previously reported MTT-based cell death data of GO-Chl exposed A549 lung cancer cells[25].

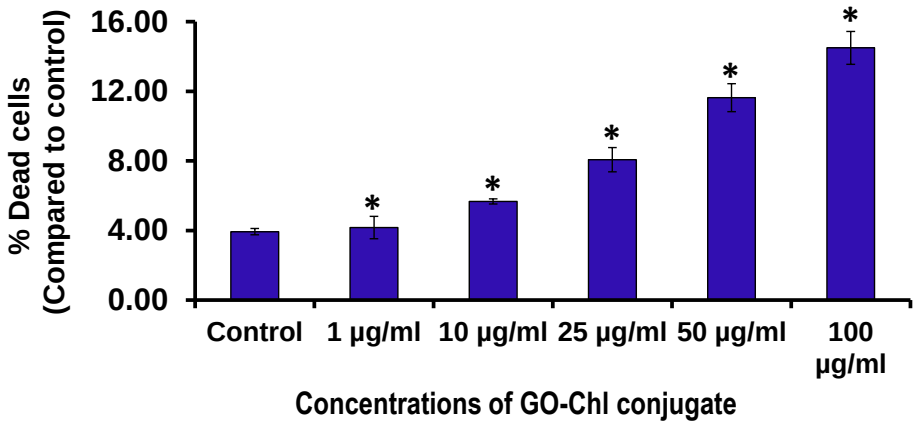

Figure 5. Flow cytometry based Propidium Iodide uptake analysis of GO-Chl exposure A549 cells: A dose dependent increase in concentration of cells with compromised cell membrane was observed. Values are expressed as mean ± SEM of three independent experiment. A value of $p<0.05$ (*) was considered as statistically significant.

3.4 Cell cycle progression analysis using flow cytometry-based PI assay

The disruption of plasma membrane integrity triggers enhanced permeability of chemotherapeutics, which leads to alterations in cell cycle, genotoxicity and autophagy modulation in cancer cells[37,52]. The cell cycle includes a division phase and an interphase which are responsible for the efficient cellular physiology and metabolic pathways. Any impairment in the cell cycle process could be used as a measure of genotoxic alterations induced by any external stresses[53]. The cell cycle process involves series of highly regulated events for cell growth, DNA replication and cell division to produce daughter cells. GO has been found to interfere with the DNA replication genes and cause alterations in cell cycle, mutagenesis and elevated DNA damage-controlled cell death in cancer cells[52]. Therefore, to access the effect of GO-Chl on cell cycle process in A549 cells we have performed flow cytometry-based cell cycle analysis. Figure 6 reveals the cell cycle analysis of GO-Chl exposed A549 cells. Results showed a significant

increase in the population of cells in sub G1 phase (reduced DNA content), which could be attributed to possible DNA fragmentation and ultimate A549 cell death by the GO-Chl nanoconjugate exposure.

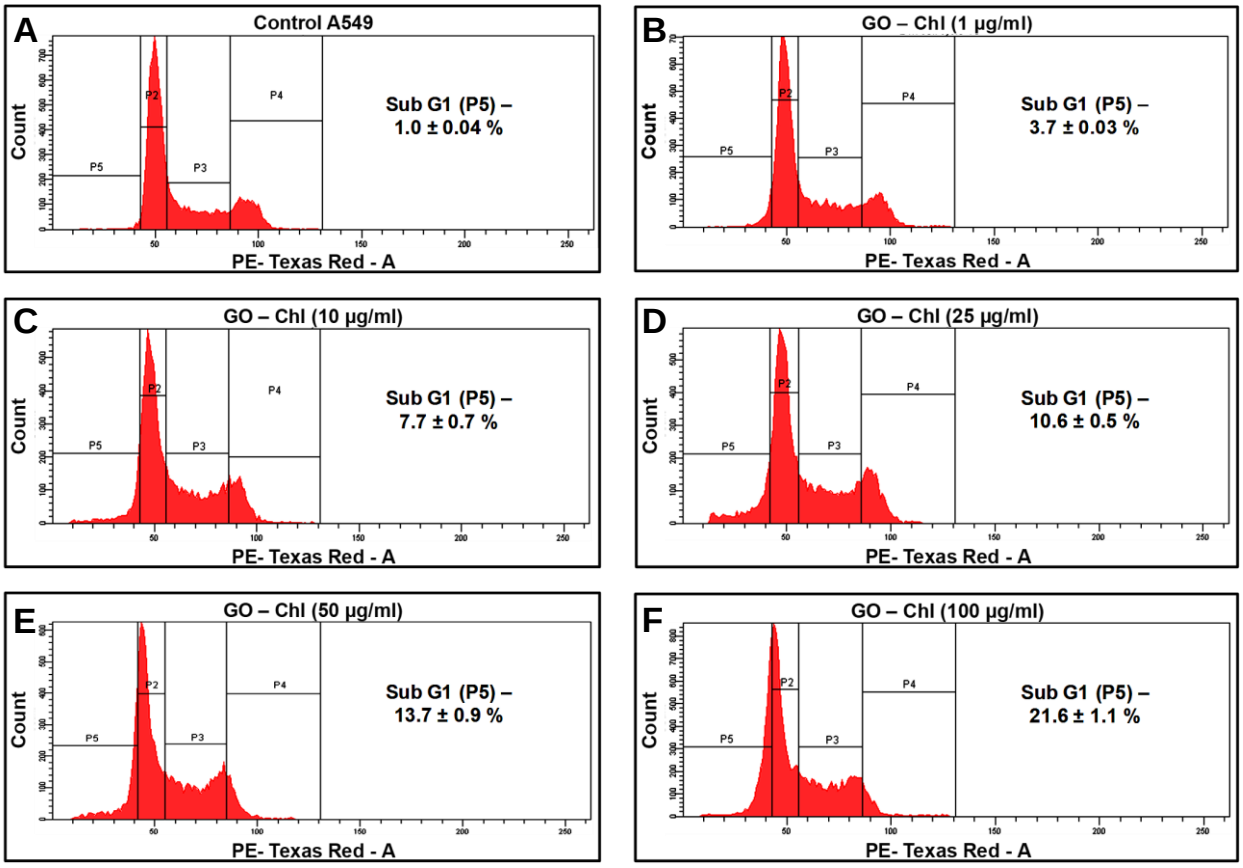

Figure 6. Flow cytometry-based cell cycle analysis of GO-Chl exposed A549 cells. Values are expressed as mean ± SEM of three independent experiments. A value of $p<0.05$ (*) was considered as statistically significant.

3.5 Genotoxicity assessment in GO-Chl exposed A549 lung cancer cells using single-cell gel electrophoresis.

To investigate the genotoxicity and DNA damage induced in GO-Chl exposed A549 lung cancer cells we performed single cell gel electrophoresis or comet assay, which is a versatile sensitive

technique to measure the single/double strand DNA breaks, DNA crosslinks, base damages and apoptotic nuclei[54]. Figure 7 reveals the DNA damage analysis in GO-Chl exposed A549 cells. In figure 7a, the digital images of DNA comets obtained by florescence microscopy indicates that GO-Chl exposure exhibits a strong genotoxic effect in A549 cells. Furthermore, a concentration-dependent increase in the tail length was observed (Figure 7b), which is a measure of the extent of DNA damage by analyzing the length of DNA migration during electrophoresis. Furthermore, statistical analysis of the resulting tail length data yielded tail DNA percentage and olive tail moment using Eq. 3 and 4, respectively.

$$\%\, DNA\ in\ tail = \frac{total\ intensity\ of\ tail}{total\ intensity\ of\ comet} \times 100 \quad (3)$$

$$Tail\ Moment = Tail\ length\ \times\ \%\, DNA\ in\ tail \quad (4)$$

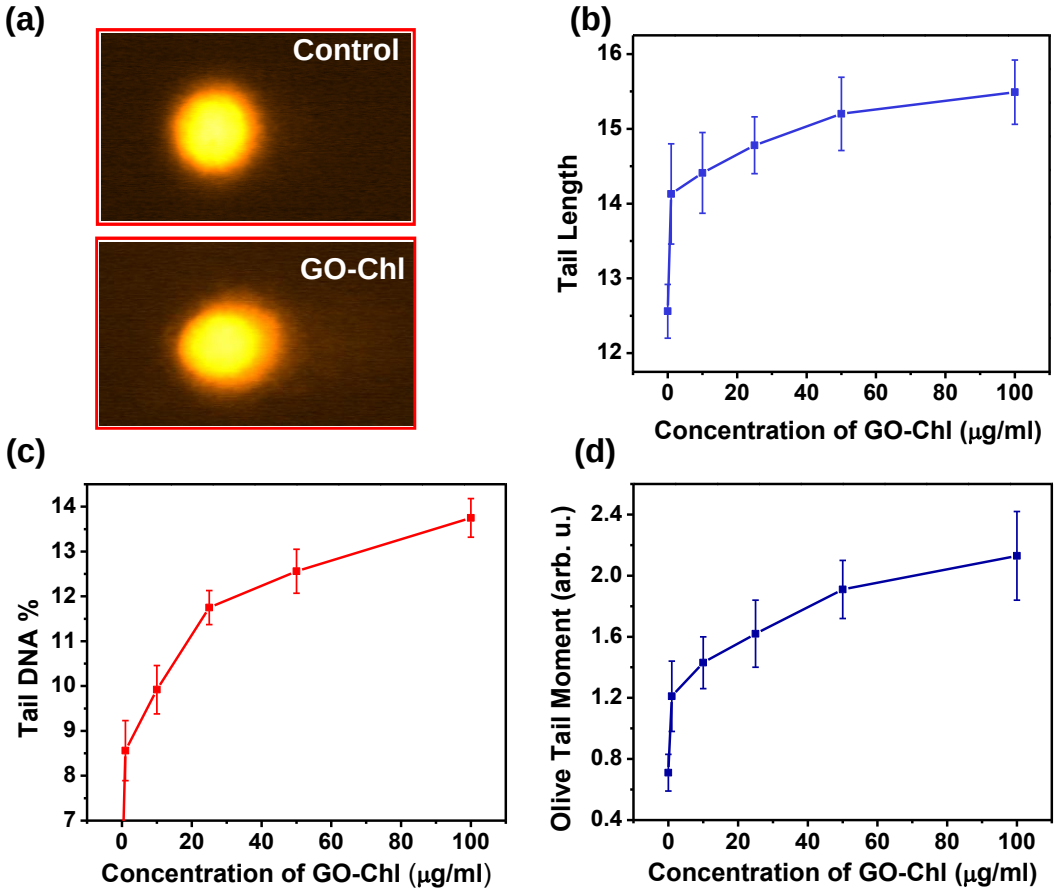

Figure 7. Comet assay of GO-Chl nanoconjugates in A549 lung cancer cells: (a) digital image of the comet formation, (b-d) concentration dependent analysis of tail length, Tail % DNA and Olive tail moment on exposure of GO-Chl in A549 lung cancer cells. Values are expressed as mean ± SEM of three independent experiments. A value of $p<0.05$ (*) was considered as statistically significant.

Figure 7b - 7d reveal a dose-dependent increase in tail length, tail DNA percentage and olive tail moment and collectively show the genotoxicity induced in GO-Chl exposed A549 cells. Recently, it was shown that exposure to higher concentrations of GO could induce DNA damage through the base excision repair (BER) pathway in HEK 293T cells[55]. The presence of high mobility and sharp edges of GO could potentially contribute towards the genotoxic behavior[55]. On the other

hand, Chl have shown its capacity for inducing genotoxicity in cancer cells in a ROS dependent manner[56]. The results indicate that induction of DNA damage in GO-Chl exposed A549 lung cancer cells could possibly be due to alteration/failure of DNA damage response mechanism.

3.6 Role of autophagy machinery in inducing DNA damage in GO-Chl exposed A549 lung cancer cells.

Cells upon exposure to external stress and endogenous metabolic changes produce variety of DNA lesions which can give rise to genomic instability via gene mutations and chromosomal damage leading to tumor progression and metastasis[57] . In a healthy cell, various DNA damage response pathways and DNA repair proteins gets activated to overcome the genetic modification caused by DNA lesions and decides the fate of cell survival and cell death[57]. In response to a particular type of DNA damage, highly selective and complex cell signaling networks like the BER pathway (for SSBs), homologous recombination repair and non-homologous end joining pathways (for DSBs), nucleotide excision repair pathways (for bulky adducts formations) and mismatch repair pathways (for nucleotide mutations) get activated to ensure cell survival[58]. During an early stage of tumorigenesis, the deregulation of cell proliferation results in loss of one or more DNA damage pathway in cancer cells leading to greater dependency on DDR. Therefore, the tendency of a cancer cell to harbor DDR dependency through activation of complex molecular signaling pathways like PARP-1 (poly-ADP ribose polymerase), DNA-dependent protein kinase (DNA-PK), activation of autophagy machinery could provide multiple target therapeutic window to treat patients with tumors lacking specific DDR functions[57,59].

In response to DNA damage and chromosomal aberrations, multi-drug resistant tumors activate the autophagy machinery as a survival mechanism[60]. However, accumulating evidence supports the fact that inhibition of autophagy by either exposure of nanomaterials or pharmacological

inhibitors could potentially inhibit the activation of DNA damage response in different cancer cells and animal models[23,61]. To elucidate the role of autophagy in DNA damage in GO-Chl exposed A549 cells, we have performed a set of experiments focusing on autophagosomes. Figure 8a, reveals the florescence microscopy-based MDC staining for labeling autophagic vacuoles in GO-Chl exposed A549 cells. The results reveal a significantly high number of acidic vacuoles (MDC positive) in GO-Chl exposed cells as compared to control cells after 24 h exposure to GO-Chl (25 µg/mL). The MDC dye selectively accumulates in autophagosomes or other acidic cellular vacuoles[32]. Therefore, to confirm the presence of autophagosomes using TEM. Figure 8b reveals the appearance of autophagosomes in GO-Chl exposed A549 cells. The MDC staining assay and TEM analysis together shows the appearance of autophagosomes, which could be due to inhibition of autophagy.

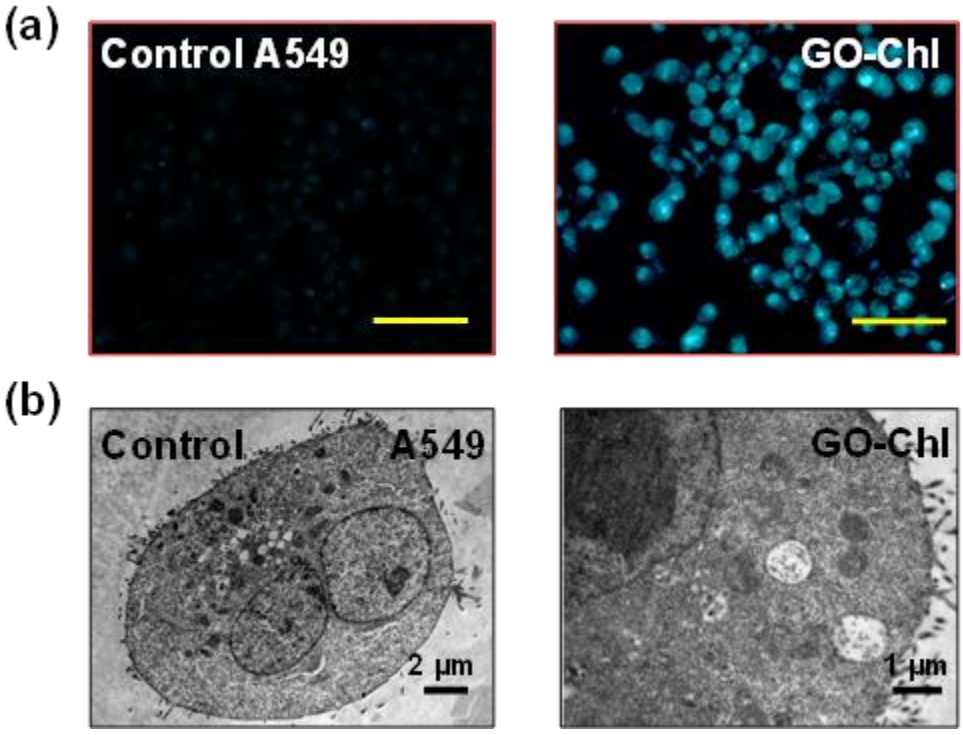

Figure 8. Accumulation of autophagosomes in GO-Chl exposed A549 lung cancer cells: (a) Monodansylcadaverine staining analysis of A549 cells exposed to GO–Chl (25 μg/mL) for the determination of acidic vacuoles (scale bar = 50 μm) and (b) Transmission electron microscope photomicrograph of GO–Chl (25 μg/mL) exposed A549 cells showing the presence of autophagosomes.

Furthermore, we performed confocal microscopy with GFP-LC3 transfected cells to investigate and quantify the accumulation of autophagosomes upon GO-Chl exposure. Mammalian LC3 is a specific marker to monitor autophagy through its incorporation into the autophagosomal membranes. During the course of autophagy, the fusion of autophagosome with lysosome results in very low LC3 content in autolysosomes due to subsequent degradation of LC3 by lysosomal enzymes[62]. Therefore, the endogenous GFP-LC3 is visualized as a diffuse cytoplasmic pool or punctate structure and could be used for the selective quantification of autophagosomes, and thus allows the monitoring of autophagy inhibition[63]. Figure 9 shows a significant increase in number of LC3 punctate and confirms the accumulation of autophagosomes in GO-Chl exposed A549 cells.

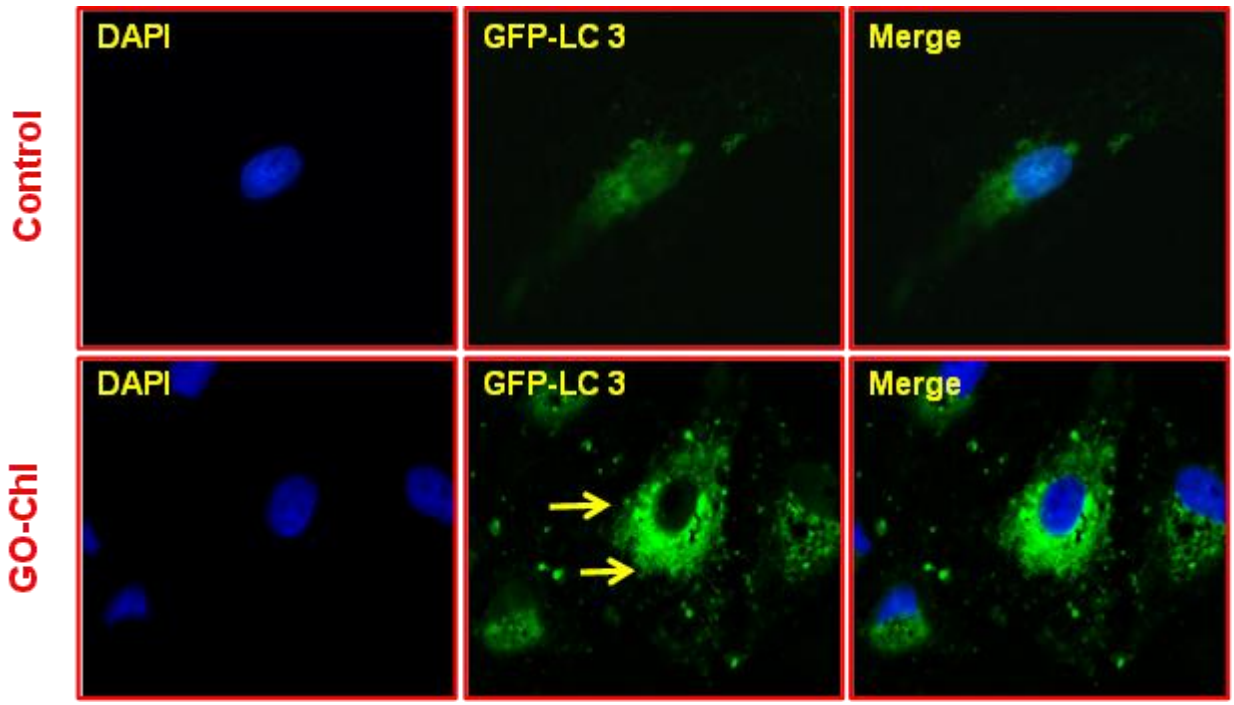

Figure 9. Mammalian GFP-LC3 transfection assay for autophagic flux analysis in GO-Chl exposed A549 cells

Autophagy requires the regulation of a number of key proteins, like Rad51, BLM/WRN DNA helicases, the Mre11 complex, or TopBP1 and DNA repairing enzymes (like DNA-PKcs, MGMT, etc.), responsible for DNA damage-associated cell death[64]. Recent studies have shown that inhibition of autophagy at different stages caused variation in the expression level of key autophagy proteins, like Beclin-1, ATG-7, LC 3-I/II and SQSTM1/p62, which could regulate the DNA damage response in cancer cells[64]. Therefore, to investigate the molecular mechanism responsible for inducing DNA damage through autophagy modulation in A549 cells upon GO-Chl nanoconjugate exposure, we performed immunoblot analysis of various related proteins. Figure 10 reveals the expression level of key autophagy proteins responsible for formation of autophagosome and functioning of autophagy process. In Figure 11, schematic representation showing the involvement of key proteins in different steps of mammalian process of autophagy.

A significant increase in the expression of Beclin-1 and ATG-7 was observed in GO-Chl exposed A549 cells. Beclin-1 is a three structure domain protein (BH-3 only, CCD, and ECD) and is key in the regulation of the mammalian autophagy process[65]. Recent studies reveal that elevated expression levels of Beclin-1 leads to enhanced DNA damage in cancer cells, leading to elevated levels of cell death[66]. On the other hand, ATG-7 is a key protein in the formation of the autophagosome through phagophore membrane elongation via activation of a ubiquitin-like conjugation system (ATG5-ATG12-ATG16)[67]. The high expression of ATG-7 protein observed points towards the formation of autophagosomes in GO-Chl exposed A549 cells and corroborates the results obtained through MDC staining and confocal microscopic analysis.

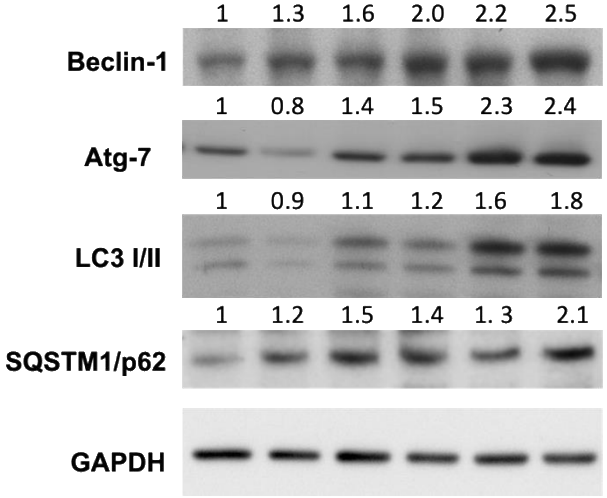

Figure 10. Western blot analysis of autophagy markers in GO-Chl exposed A549 cells lysate in a dose (μg/mL) dependent manner. Values are expressed as mean ± SEM of three independent experiments. A value of $p<0.05$ (*) is considered as statistically significant.

Furthermore, a significant dose-dependent increase in the expression level of LC-3 II proteins was observed. LC-3 is a microtubule associated protein 1A/1B – light chain 3 (LC-3) that becomes

lipidated and tightly associated with the autophagosome membrane[68]. LC-3 proteins are incorporated onto the autophagosome membrane, which is later degraded by autolysosomes (formed by fusion of autophagosome and lysosome)[69]. Elevated expression of LC-3 I/II biomarkers indicate the formation and accumulation of autophagosomes and suggests the inhibition of autophagy in GO-Chl exposed A549 cells.

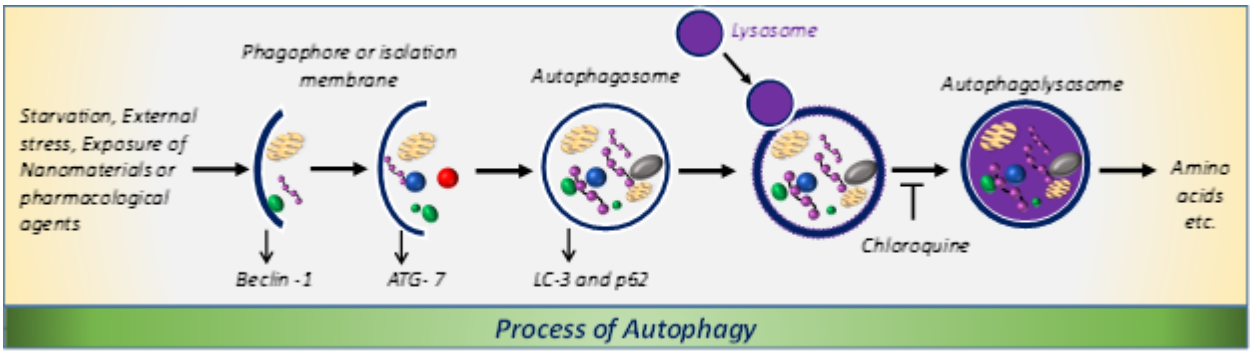

Figure 11. Schematic showing the mammalian process of autophagy and modulation of autophagy by chloroquine by inhibiting the fusion of autophagosome and lysosome.

In addition, a significant increase in the expression levels of SQSTM1/p62 was observed, demonstrating the modulation of autophagy at a later stage by inhibiting the fusion of autophagosome with lysosomes. SQSTM1/p62 is a multi-domain protein that interacts with the autophagy machinery to regulate various cellular metabolism processes[70]. Recent studies reveals the importance of p62 in regulating the mode of cell death process, harnessing the DNA damage response capability and inducing complex signaling networks responsible for cellular detoxification[70,71]. Most importantly, it was found that the autophagy substrate SQSTM1/p62 inhibits the E3 ligase RNF168-dependent ubiquitination of chromatin and plays a crucial role in dysfunction of DNA repair capacity through autophagy modulation[22]. The elevated expression of p62 observed in the present study is in good agreement with the previously reported data,

suggesting the critical role of the autophagy machinery in harnessing the DNA damage response in GO-Chl exposed A549 cells. However, a detailed mechanistic investigation of the key check points will be required. Therefore, from the available literature and experimental observations from present study, it becomes clear that the autophagy machinery plays an important role in regulating the DNA damage response in A549 cells and that the GO-Chl nanoconjugate can induce the DNA damage through SQSTM1/p62 mediated autophagy modulation.

4. Conclusion

We have successfully demonstrated the genotoxicity induced in A549 lung cancer cells by exposure to the GO-Chl nanoconjugate and clarified the role of autophagy modulation in harnessing the DNA damage response. Flow cytometry-based PI uptake reveals a significant loss of plasma membrane integrity, which leads to cell cycle arrest. Furthermore, single cell gel electrophoresis or comet assay reveals a significant dose-dependent increase in tail length, tail DNA percentage and olive tail moment as a measurement of genotoxicity in GO-Chl exposed A549 cells.

To access the role of autophagy modulation in GO-Chl nanoconjugate we have employed MDC staining, GFP-LC3 plasmid based confocal microscopic and TEM analysis. A significant dose-dependent increase accumulation of autophagosomes was observed, suggesting inhibition of autophagy and the possible connection between DNA damage response and autophagy. Finally, elevated expression levels of key autophagy proteins Beclin-1, ATG-7, LC3- I/II and SQSTM1/p62 reveal that inhibition of autophagy at later stages plays a crucial role in regulating the DNA damage response capability in GO-Chl exposed A549 cells. These result reveal the efficacy of GO-Chl nanoconjugate as a nanodrug candidate alone or in combination with other chemotherapeutic drugs through unique DNA damage-autophagy synergy.

Acknowledgement

The Director of the CSIR-National Physical Laboratory, New Delhi, and Director of the CSIR-Indian Institute of Toxicology Research, Lucknow are gratefully acknowledged for their strong interest and support to this work. BDA and SM sincerely acknowledge Mr. Jai Shankar, Mr. Dinesh, Dr. Monu Mishra and Mr. Jai Tavale for instrumental analysis. BDA and SPS duly acknowledge the employment of various software like Avogadro (http://avogadro.cc/), Microsoft PowerPoint, and Mind The Graph for preparation of schematic and graphical abstracts in the present study. Graphical Abstract was created using the "Mind the Graph" tool (https://mindthegraph.com/). This content is not subject to CC BY 4.0.

Funding Statement

The authors declare that this study was supported by the funding obtained from Indo-Us Joint Centre of Nanomedicine for Head & Neck Cancer/34-2012/2015-16.

Conflict of Interest

The authors declare no conflict of interest.

References

(1) Siegel, R. L.; Giaquinto, A. N.; Jemal, A. Cancer Statistics, 2024. *CA. Cancer J. Clin.* **2024**, *74* (1), 12–49. https://doi.org/10.3322/caac.21820.

(2) Holohan, C.; Van Schaeybroeck, S.; Longley, D. B.; Johnston, P. G. Cancer Drug Resistance: An Evolving Paradigm. *Nat. Rev. Cancer* **2013**, *13* (10), 714–726. https://doi.org/10.1038/nrc3599.

(3) Yuan, S.; Almagro, J.; Fuchs, E. Beyond Genetics: Driving Cancer with the Tumour Microenvironment behind the Wheel. *Nat. Rev. Cancer* **2024**, *24* (4), 274–286. https://doi.org/10.1038/s41568-023-00660-9.

(4) Iqbal, M. J.; Kabeer, A.; Abbas, Z.; Siddiqui, H. A.; Calina, D.; Sharifi-Rad, J.; Cho, W. C. Interplay of Oxidative Stress, Cellular Communication and Signaling Pathways in Cancer. *Cell Commun. Signal.* **2024**, *22* (1), 7. https://doi.org/10.1186/s12964-023-01398-5.

(5) Woods, D.; Turchi, J. J. Chemotherapy Induced DNA Damage Response: Convergence of Drugs and Pathways. *Cancer Biol. Ther.* **2013**, *14* (5), 379–389. https://doi.org/10.4161/cbt.23761.

(6) Huang, R.-X.; Zhou, P.-K. DNA Damage Response Signaling Pathways and Targets for Radiotherapy Sensitization in Cancer. *Signal Transduct. Target. Ther.* **2020**, *5* (1), 60. https://doi.org/10.1038/s41392-020-0150-x.

(7) Walweel, N.; Aydin, O. Enhancing Therapeutic Efficacy in Cancer Treatment: Integrating Nanomedicine with Autophagy Inhibition Strategies. *ACS Omega* **2024**, *9* (26), 27832–27852. https://doi.org/10.1021/acsomega.4c02234.

(8) Singh, N.; Nelson, B.; Scanlan, L.; Coskun, E.; Jaruga, P.; Doak, S. Exposure to Engineered Nanomaterials: Impact on DNA Repair Pathways. *Int. J. Mol. Sci.* **2017**, *18* (7), 1515. https://doi.org/10.3390/ijms18071515.

(9) Jangili, P.; Kong, N.; Kim, J. H.; Zhou, J.; Liu, H.; Zhang, X.; Tao, W.; Kim, J. S. DNA-Damage-Response-Targeting Mitochondria-Activated Multifunctional Prodrug Strategy for Self-Defensive Tumor Therapy. *Angew. Chem. Int. Ed.* **2022**, *61* (16). https://doi.org/10.1002/anie.202117075.

(10) Zheng, X.; Song, X.; Zhu, G.; Pan, D.; Li, H.; Hu, J.; Xiao, K.; Gong, Q.; Gu, Z.; Luo, K.; Li, W. Nanomedicine Combats Drug Resistance in Lung Cancer. *Adv. Mater.* **2024**, *36* (3), 2308977. https://doi.org/10.1002/adma.202308977.

(11) Satapathy, S. R.; Mohapatra, P.; Preet, R.; Das, D.; Sarkar, B.; Choudhuri, T.; Wyatt, M. D.; Kundu, C. N. Silver-Based Nanoparticles Induce Apoptosis in Human Colon Cancer Cells Mediated through P53. *Nanomed.* **2013**, *8* (8), 1307–1322. https://doi.org/10.2217/nnm.12.176.

(12) Papa, A.-L.; Basu, S.; Sengupta, P.; Banerjee, D.; Sengupta, S.; Harfouche, R. Mechanistic Studies of Gemcitabine-Loaded Nanoplatforms in Resistant Pancreatic Cancer Cells. *BMC Cancer* **2012**, *12* (1), 419. https://doi.org/10.1186/1471-2407-12-419.

(13) Armand, L.; Biola-Clier, M.; Bobyk, L.; Collin-Faure, V.; Diemer, H.; Strub, J.-M.; Cianferani, S.; Van Dorsselaer, A.; Herlin-Boime, N.; Rabilloud, T.; Carriere, M. Molecular Responses of Alveolar Epithelial A549 Cells to Chronic Exposure to Titanium Dioxide Nanoparticles: A Proteomic View. *J. Proteomics* **2016**, *134*, 163–173. https://doi.org/10.1016/j.jprot.2015.08.006.

(14) Bai, D.-P.; Zhang, X.-F.; Zhang, G.-L.; Huang, Y.-F.; Gurunathan, S. Zinc Oxide Nanoparticles Induce Apoptosis and Autophagy in Human Ovarian Cancer Cells. *Int. J. Nanomedicine* **2017**, *Volume 12*, 6521–6535. https://doi.org/10.2147/IJN.S140071.

(15) Lin, K.-C.; Lin, M.-W.; Hsu, M.-N.; Yu-Chen, G.; Chao, Y.-C.; Tuan, H.-Y.; Chiang, C.-S.; Hu, Y.-C. Graphene Oxide Sensitizes Cancer Cells to Chemotherapeutics by Inducing Early Autophagy Events, Promoting Nuclear Trafficking and Necrosis. *Theranostics* **2018**, *8* (9), 2477–2487. https://doi.org/10.7150/thno.24173.

(16) Qi, L.; Pan, T.; Ou, L.; Ye, Z.; Yu, C.; Bao, B.; Wu, Z.; Cao, D.; Dai, L. Biocompatible Nucleus-Targeted Graphene Quantum Dots for Selective Killing of Cancer Cells via DNA Damage. *Commun. Biol.* **2021**, *4* (1), 214. https://doi.org/10.1038/s42003-021-01713-1.
(17) Barba-Rosado, L. V.; Carrascal-Hernández, D. C.; Insuasty, D.; Grande-Tovar, C. D. Graphene Oxide (GO) for the Treatment of Bone Cancer: A Systematic Review and Bibliometric Analysis. *Nanomaterials* **2024**, *14* (2), 186. https://doi.org/10.3390/nano14020186.
(18) Chen, G.-Y.; Chen, C.-L.; Tuan, H.-Y.; Yuan, P.-X.; Li, K.-C.; Yang, H.-J.; Hu, Y.-C. Graphene Oxide Triggers Toll-Like Receptors/Autophagy Responses In Vitro and Inhibits Tumor Growth In Vivo. *Adv. Healthc. Mater.* **2014**, *3* (9), 1486–1495. https://doi.org/10.1002/adhm.201300591.
(19) Feng, X.; Chen, L.; Guo, W.; Zhang, Y.; Lai, X.; Shao, L.; Li, Y. Graphene Oxide Induces P62/SQSTM-Dependent Apoptosis through the Impairment of Autophagic Flux and Lysosomal Dysfunction in PC12 Cells. *Acta Biomater.* **2018**, *81*, 278–292. https://doi.org/10.1016/j.actbio.2018.09.057.
(20) Fiorillo, M.; Verre, A. F.; Iliut, M.; Peiris-Pagés, M.; Ozsvari, B.; Gandara, R.; Cappello, A. R.; Sotgia, F.; Vijayaraghavan, A.; Lisanti, M. P. Graphene Oxide Selectively Targets Cancer Stem Cells, across Multiple Tumor Types: Implications for Non-Toxic Cancer Treatment, via "Differentiation-Based Nano-Therapy." *Oncotarget* **2015**, *6* (6), 3553–3562. https://doi.org/10.18632/oncotarget.3348.
(21) Zhu, J.; Xu, M.; Gao, M.; Zhang, Z.; Xu, Y.; Xia, T.; Liu, S. Graphene Oxide Induced Perturbation to Plasma Membrane and Cytoskeletal Meshwork Sensitize Cancer Cells to Chemotherapeutic Agents. *ACS Nano* **2017**, *11* (3), 2637–2651. https://doi.org/10.1021/acsnano.6b07311.
(22) Wang, Y.; Zhang, N.; Zhang, L.; Li, R.; Fu, W.; Ma, K.; Li, X.; Wang, L.; Wang, J.; Zhang, H.; Gu, W.; Zhu, W.-G.; Zhao, Y. Autophagy Regulates Chromatin Ubiquitination in DNA Damage Response through Elimination of SQSTM1/P62. *Mol. Cell* **2016**, *63* (1), 34–48. https://doi.org/10.1016/j.molcel.2016.05.027.
(23) Mei, L.; Zhang, X.; Feng, S.-S. Autophagy Inhibition Strategy for Advanced Nanomedicine. *Nanomed.* **2014**, *9* (3), 377–380. https://doi.org/10.2217/nnm.13.218.
(24) Kim, J.; Lee, S.; Kim, H.; Lee, H.; Seong, K. M.; Youn, H.; Youn, B. Autophagic Organelles in DNA Damage Response. *Front. Cell Dev. Biol.* **2021**, *9*, 668735. https://doi.org/10.3389/fcell.2021.668735.
(25) Arya, B. D.; Mittal, S.; Joshi, P.; Pandey, A. K.; Ramirez-Vick, J. E.; Singh, S. P. Graphene Oxide–Chloroquine Nanoconjugate Induce Necroptotic Death in A549 Cancer Cells through Autophagy Modulation. *Nanomed.* **2018**, *13* (18), 2261–2282. https://doi.org/10.2217/nnm-2018-0086.
(26) Hummers, W. S.; Offeman, R. E. Preparation of Graphitic Oxide. *J. Am. Chem. Soc.* **1958**, *80* (6), 1339–1339. https://doi.org/10.1021/ja01539a017.
(27) Cote, L. J.; Kim, F.; Huang, J. Langmuir−Blodgett Assembly of Graphite Oxide Single Layers. *J. Am. Chem. Soc.* **2009**, *131* (3), 1043–1049. https://doi.org/10.1021/ja806262m.
(28) Dimiev, A.; Kosynkin, D. V.; Alemany, L. B.; Chaguine, P.; Tour, J. M. Pristine Graphite Oxide. *J. Am. Chem. Soc.* **2012**, *134* (5), 2815–2822. https://doi.org/10.1021/ja211531y.
(29) Crowley, L. C.; Scott, A. P.; Marfell, B. J.; Boughaba, J. A.; Chojnowski, G.; Waterhouse, N. J. Measuring Cell Death by Propidium Iodide Uptake and Flow Cytometry. *Cold Spring Harb. Protoc.* **2016**, *2016* (7), pdb.prot087163. https://doi.org/10.1101/pdb.prot087163.
(30) Singh, N. P.; Muller, C. H.; Berger, R. E. Effects of Age on DNA Double-Strand Breaks and Apoptosis in Human Sperm. *Fertil. Steril.* **2003**, *80* (6), 1420–1430. https://doi.org/10.1016/j.fertnstert.2003.04.002.
(31) Bajpayee, M.; Kumar, A.; Dhawan, A. Chapter 1. The Comet Assay: A Versatile Tool for Assessing DNA Damage. In *Issues in Toxicology*; Royal Society of Chemistry: Cambridge, 2016; pp 1–64. https://doi.org/10.1039/9781782622895-00001.
(32) Munafó, D. B.; Colombo, M. I. A Novel Assay to Study Autophagy: Regulation of Autophagosome Vacuole Size by Amino Acid Deprivation. *J. Cell Sci.* **2001**, *114* (Pt 20), 3619–3629.

(33) Pugsley, H. R. Quantifying Autophagy: Measuring LC3 Puncta and Autolysosome Formation in Cells Using Multispectral Imaging Flow Cytometry. *Methods* **2017**, *112*, 147–156. https://doi.org/10.1016/j.ymeth.2016.05.022.
(34) Bradford, M. M. A Rapid and Sensitive Method for the Quantitation of Microgram Quantities of Protein Utilizing the Principle of Protein-Dye Binding. *Anal. Biochem.* **1976**, *72*, 248–254.
(35) Shen, L.; Zhang, L.; Wang, K.; Miao, L.; Lan, Q.; Jiang, K.; Lu, H.; Li, M.; Li, Y.; Shen, B.; Zheng, W. Analysis of Oxidation Degree of Graphite Oxide and Chemical Structure of Corresponding Reduced Graphite Oxide by Selecting Different-Sized Original Graphite. *RSC Adv.* **2018**, *8* (31), 17209–17217. https://doi.org/10.1039/C8RA01486H.
(36) Zhang, W.; Yan, L.; Li, M.; Zhao, R.; Yang, X.; Ji, T.; Gu, Z.; Yin, J.-J.; Gao, X.; Nie, G. Deciphering the Underlying Mechanisms of Oxidation-State Dependent Cytotoxicity of Graphene Oxide on Mammalian Cells. *Toxicol. Lett.* **2015**, *237* (2), 61–71. https://doi.org/10.1016/j.toxlet.2015.05.021.
(37) Li, R.; Guiney, L. M.; Chang, C. H.; Mansukhani, N. D.; Ji, Z.; Wang, X.; Liao, Y.-P.; Jiang, W.; Sun, B.; Hersam, M. C.; Nel, A. E.; Xia, T. Surface Oxidation of Graphene Oxide Determines Membrane Damage, Lipid Peroxidation, and Cytotoxicity in Macrophages in a Pulmonary Toxicity Model. *ACS Nano* **2018**, *12* (2), 1390–1402. https://doi.org/10.1021/acsnano.7b07737.
(38) Hanwell, M. D.; Curtis, D. E.; Lonie, D. C.; Vandermeersch, T.; Zurek, E.; Hutchison, G. R. Avogadro: An Advanced Semantic Chemical Editor, Visualization, and Analysis Platform. *J. Cheminformatics* **2012**, *4* (1), 17. https://doi.org/10.1186/1758-2946-4-17.
(39) Lai, Q.; Zhu, S.; Luo, X.; Zou, M.; Huang, S. Ultraviolet-Visible Spectroscopy of Graphene Oxides. *AIP Adv.* **2012**, *2* (3), 032146. https://doi.org/10.1063/1.4747817.
(40) Joshi, P.; Chakraborty, S.; Dey, S.; Shanker, V.; Ansari, Z. A.; Singh, S. P.; Chakrabarti, P. Binding of Chloroquine–Conjugated Gold Nanoparticles with Bovine Serum Albumin. *J. Colloid Interface Sci.* **2011**, *355* (2), 402–409. https://doi.org/10.1016/j.jcis.2010.12.032.
(41) Rattana; Chaiyakun, S.; Witit-anun, N.; Nuntawong, N.; Chindaudom, P.; Oaew, S.; Kedkeaw, C.; Limsuwan, P. Preparation and Characterization of Graphene Oxide Nanosheets. *Procedia Eng.* **2012**, *32*, 759–764. https://doi.org/10.1016/j.proeng.2012.02.009.
(42) Navarro, M.; Hernández, C.; Vásquez, F.; Goitia, H.; Ojeda, L. E.; Velásquez, M.; Fraile, G. Syntheses, Characterization, and Biological Evaluation of New Zinc-and Gold-Chloroquine Diphosphate Complexes. *Transit. Met. Chem.* **2008**, *33* (7), 893–898. https://doi.org/10.1007/s11243-008-9129-0.
(43) Krishnamoorthy, K.; Veerapandian, M.; Yun, K.; Kim, S.-J. The Chemical and Structural Analysis of Graphene Oxide with Different Degrees of Oxidation. *Carbon* **2013**, *53*, 38–49. https://doi.org/10.1016/j.carbon.2012.10.013.
(44) Drewniak, S.; Muzyka, R.; Stolarczyk, A.; Pustelny, T.; Kotyczka-Morańska, M.; Setkiewicz, M. Studies of Reduced Graphene Oxide and Graphite Oxide in the Aspect of Their Possible Application in Gas Sensors. *Sensors* **2016**, *16* (1), 103. https://doi.org/10.3390/s16010103.
(45) Wang, J.; Salihi, E. C.; Šiller, L. Green Reduction of Graphene Oxide Using Alanine. *Mater. Sci. Eng. C* **2017**, *72*, 1–6. https://doi.org/10.1016/j.msec.2016.11.017.
(46) Song, J.; Wang, X.; Chang, C.-T. Preparation and Characterization of Graphene Oxide. *J. Nanomater.* **2014**, *2014*, 1–6. https://doi.org/10.1155/2014/276143.
(47) Gao, W.; Alemany, L. B.; Ci, L.; Ajayan, P. M. New Insights into the Structure and Reduction of Graphite Oxide. *Nat. Chem.* **2009**, *1* (5), 403–408. https://doi.org/10.1038/nchem.281.
(48) Wilson, N. R.; Pandey, P. A.; Beanland, R.; Young, R. J.; Kinloch, I. A.; Gong, L.; Liu, Z.; Suenaga, K.; Rourke, J. P.; York, S. J.; Sloan, J. Graphene Oxide: Structural Analysis and Application as a Highly Transparent Support for Electron Microscopy. *ACS Nano* **2009**, *3* (9), 2547–2556. https://doi.org/10.1021/nn900694t.

(49) Rivolta, I.; Panariti; Miserocchi. The Effect of Nanoparticle Uptake on Cellular Behavior: Disrupting or Enabling Functions? *Nanotechnol. Sci. Appl.* **2012**, 87. https://doi.org/10.2147/NSA.S25515.
(50) Piperno, A.; Scala, A.; Mazzaglia, A.; Neri, G.; Pennisi, R.; Sciortino, M.; Grassi, G. Cellular Signaling Pathways Activated by Functional Graphene Nanomaterials. *Int. J. Mol. Sci.* **2018**, *19* (11), 3365. https://doi.org/10.3390/ijms19113365.
(51) Bernardes, N.; Fialho, A. Perturbing the Dynamics and Organization of Cell Membrane Components: A New Paradigm for Cancer-Targeted Therapies. *Int. J. Mol. Sci.* **2018**, *19* (12), 3871. https://doi.org/10.3390/ijms19123871.
(52) Liu, Y.; Luo, Y.; Wu, J.; Wang, Y.; Yang, X.; Yang, R.; Wang, B.; Yang, J.; Zhang, N. Graphene Oxide Can Induce in Vitro and in Vivo Mutagenesis. *Sci. Rep.* **2013**, *3* (1), 3469. https://doi.org/10.1038/srep03469.
(53) Wei, K. Y.; Smolke, C. D. Engineering Dynamic Cell Cycle Control with Synthetic Small Molecule-Responsive RNA Devices. *J. Biol. Eng.* **2015**, *9* (1), 21. https://doi.org/10.1186/s13036-015-0019-7.
(54) Olive, P. L.; Banáth, J. P. The Comet Assay: A Method to Measure DNA Damage in Individual Cells. *Nat. Protoc.* **2006**, *1* (1), 23–29. https://doi.org/10.1038/nprot.2006.5.
(55) Lu, C.-J.; Jiang, X.-F.; Junaid, M.; Ma, Y.-B.; Jia, P.-P.; Wang, H.-B.; Pei, D.-S. Graphene Oxide Nanosheets Induce DNA Damage and Activate the Base Excision Repair (BER) Signaling Pathway Both in Vitro and in Vivo. *Chemosphere* **2017**, *184*, 795–805. https://doi.org/10.1016/j.chemosphere.2017.06.049.
(56) Hu, T.; Li, P.; Luo, Z.; Chen, X.; Zhang, J.; Wang, C.; Chen, P.; Dong, Z. Chloroquine Inhibits Hepatocellular Carcinoma Cell Growth in Vitro and in Vivo. *Oncol. Rep.* **2016**, *35* (1), 43–49. https://doi.org/10.3892/or.2015.4380.
(57) Roos, W. P.; Thomas, A. D.; Kaina, B. DNA Damage and the Balance between Survival and Death in Cancer Biology. *Nat. Rev. Cancer* **2016**, *16* (1), 20–33. https://doi.org/10.1038/nrc.2015.2.
(58) Hosoya, N.; Miyagawa, K. Targeting DNA Damage Response in Cancer Therapy. *Cancer Sci.* **2014**, *105* (4), 370–388. https://doi.org/10.1111/cas.12366.
(59) Eliopoulos, A. G.; Havaki, S.; Gorgoulis, V. G. DNA Damage Response and Autophagy: A Meaningful Partnership. *Front. Genet.* **2016**, *7*. https://doi.org/10.3389/fgene.2016.00204.
(60) Vanzo, R.; Bartkova, J.; Merchut-Maya, J. M.; Hall, A.; Bouchal, J.; Dyrskjøt, L.; Frankel, L. B.; Gorgoulis, V.; Maya-Mendoza, A.; Jäättelä, M.; Bartek, J. Autophagy Role(s) in Response to Oncogenes and DNA Replication Stress. *Cell Death Differ.* **2020**, *27* (3), 1134–1153. https://doi.org/10.1038/s41418-019-0403-9.
(61) Gomes, L.; Menck, C.; Leandro, G. Autophagy Roles in the Modulation of DNA Repair Pathways. *Int. J. Mol. Sci.* **2017**, *18* (11), 2351. https://doi.org/10.3390/ijms18112351.
(62) Yim, W. W.-Y.; Mizushima, N. Lysosome Biology in Autophagy. *Cell Discov.* **2020**, *6* (1), 6. https://doi.org/10.1038/s41421-020-0141-7.
(63) Mizushima, N.; Yoshimori, T.; Levine, B. Methods in Mammalian Autophagy Research. *Cell* **2010**, *140* (3), 313–326. https://doi.org/10.1016/j.cell.2010.01.028.
(64) Zhang, D.; Tang, B.; Xie, X.; Xiao, Y.-F.; Yang, S.-M.; Zhang, J.-W. The Interplay between DNA Repair and Autophagy in Cancer Therapy. *Cancer Biol. Ther.* **2015**, *16* (7), 1005–1013. https://doi.org/10.1080/15384047.2015.1046022.
(65) Kang, R.; Zeh, H. J.; Lotze, M. T.; Tang, D. The Beclin 1 Network Regulates Autophagy and Apoptosis. *Cell Death Differ.* **2011**, *18* (4), 571–580. https://doi.org/10.1038/cdd.2010.191.
(66) Zhu, J.; Cai, Y.; Xu, K.; Ren, X.; Sun, J.; Lu, S.; Chen, J.; Xu, P. Beclin1 Overexpression Suppresses Tumor Cell Proliferation and Survival via an Autophagy-dependent Pathway in Human Synovial Sarcoma Cells. *Oncol. Rep.* **2018**. https://doi.org/10.3892/or.2018.6599.

(67) Ye, X.; Zhou, X.-J.; Zhang, H. Exploring the Role of Autophagy-Related Gene 5 (ATG5) Yields Important Insights Into Autophagy in Autoimmune/Autoinflammatory Diseases. *Front. Immunol.* **2018**, *9*, 2334. https://doi.org/10.3389/fimmu.2018.02334.
(68) Hansen, T. E.; Johansen, T. Following Autophagy Step by Step. *BMC Biol.* **2011**, *9* (1), 39. https://doi.org/10.1186/1741-7007-9-39.
(69) Niklaus, M.; Adams, O.; Berezowska, S.; Zlobec, I.; Graber, F.; Slotta-Huspenina, J.; Nitsche, U.; Rosenberg, R.; Tschan, M. P.; Langer, R. Expression Analysis of LC3B and P62 Indicates Intact Activated Autophagy Is Associated with an Unfavorable Prognosis in Colon Cancer. *Oncotarget* **2017**, *8* (33), 54604–54615. https://doi.org/10.18632/oncotarget.17554.
(70) Islam, Md.; Sooro, M.; Zhang, P. Autophagic Regulation of P62 Is Critical for Cancer Therapy. *Int. J. Mol. Sci.* **2018**, *19* (5), 1405. https://doi.org/10.3390/ijms19051405.
(71) Goodall, M. L.; Fitzwalter, B. E.; Zahedi, S.; Wu, M.; Rodriguez, D.; Mulcahy-Levy, J. M.; Green, D. R.; Morgan, M.; Cramer, S. D.; Thorburn, A. The Autophagy Machinery Controls Cell Death Switching between Apoptosis and Necroptosis. *Dev. Cell* **2016**, *37* (4), 337–349. https://doi.org/10.1016/j.devcel.2016.04.018.